


Cite this: *RSC Adv.*, 2020, **10**, 29119

A cobalt–pyrrole coordination compound as high performance cathode catalyst for direct borohydride fuel cells

Yuehan Chen, ^{*ab} Shuping Wang^{ab} and Zhoupeng Li ^{*ab}

Pyrrole and cobalt nitrate were used as nitrogen and metal sources respectively to synthesize a dinitratobis(polypyrrole)cobalt(II) ($\text{Co}(\text{polypyrrole})_2(\text{NO}_3)_2$) adduct as the precursor of a Co–pyrrole/MPC catalyst. Pyrrole has the capability of polymerization and coordination with Co(II). Taking this advantage, the $\text{Co}(\text{polypyrrole})_2(\text{NO}_3)_2$ coordination can form a long-chain structure with abundant and robust Co–N bonds, contributing to significantly increased catalytic sites in the product catalyst. As a result, the obtained Co–pyrrole/MPC (MPC = macroporous carbon) catalyst exhibited high ORR catalytic activity in alkaline media and excellent performance in direct borohydride fuel cell (DBFC). A peak power density up to 325 mW cm^{-2} was achieved at ambient condition, outperforming the commercialized Pt/XC-72 benchmark containing 28.6 wt% Pt. The construction of long-chain coordination precursor was verified playing a key role in the electrochemical improvement of Co–pyrrole/MPC catalyst in DBFC.

Received 11th June 2020

Accepted 25th July 2020

DOI: 10.1039/d0ra05143h

rsc.li/rsc-advances

1. Introduction

With intriguing merits such as environmental friendliness and high energy conversion efficiency, fuel cells have attracted wide attention in the development of clean and efficient energy technologies. The performance of a fuel cells highly depends on the cathode catalyst where the oxygen reduction reaction (ORR) occurs. Expensive platinum (Pt) and Pt containing alloys are the best electrocatalysts for ORR,¹ however, the scarcity of Pt in nature is seriously impeding the commercialization of Pt-based fuel cells, so discovering ORR catalysts with low cost and high activity is the key solution to cell development. Nowadays, non-Pt catalysts have attracted much attention owing to their great affordability and decent catalytic performance.² Numerous non-Pt ORR catalysts have been developed, including polyoxometalates,³ metal oxides,⁴ metal-macrocyclic compound,^{5–7} metal doped polymers,^{8,9} etc. High performance ORR catalyst requires high catalytic activity, including the intrinsic activity as well as the number of the active sites.^{10,11} Given this, porous non-Pt catalysts are considered as highly promising alternatives to Pt due to their cost effectiveness and high surface area, which is capable of loading more catalytic sites to compensate the inferiority in intrinsic catalytic activity.^{12–14}

Among the various candidates, M–N/MPC (M = transition metal, N = nitrogenous compound, MPC = microporous

carbon) catalysts show a particular potential as high-performance ORR catalysts to replace Pt.^{15–17} MPC has higher specific surface area and can support more active centers than the common carbon materials. Generally, the M–N_x sites are widely considered as the catalytic centers for ORR.^{18–21} Pyrrolic N with unpaired electrons provides excellent coordination capability with transition metals to form macrocyclic compounds such as metallo-phthalocyanines and -porphyrins, in which the M–N_x moiety is the active site for ORR.^{22–24} Metal complexes of N₄-macrocycles such as porphyrins have been studied as alternatives to Pt catalyst.²⁵ In view of this, we attempted to synthesize a unique dinitratobis(polypyrrole)cobalt(II) ($\text{Co}(\text{polypyrrole})_2(\text{NO}_3)_2$) coordination by using pyrrole and cobalt nitrate as nitrogen and metal sources, respectively. The coordination was further employed as precursor in rich of M–N_x moieties for the preparation of highly active ORR catalyst. Cobalt nitrate can be easily coordinated with two heterocyclic ligands to form bidentate nitroato-complexes ($\text{CoL}_2(\text{NO}_3)_2$).^{26–28} Co element can improve the chemical and physical properties of the electrocatalyst, including good conductivity, abundant valid active sites and large specific surface.^{29–31} The good catalytic activity towards ORR benefits from the Co–N bond. Moreover, pyrrole delivers sufficient pyrrolic N for such coordination, while the good polymerizability of pyrrole renders a promising precursor structure towards M–N_x catalyst with sufficient active sites.^{32–35}

Upon the coordination, the limitation of pyrrole solubility in aqueous media was overcome through the use of glucose as a hydrotropic agent benefiting from its hydrolysis that generated hydroxymethylfurfural to enhance the hydrotropic effect on pyrrole dissolution.³⁶ Meanwhile, glucose also acted as the

^aZhejiang Provincial Key Laboratory of Advanced Chemical Engineering Manufacture Technology, Zhejiang University, Hangzhou 310027, China. E-mail: 541809696@qq.com; zhoupengli@zju.edu.cn; Tel: +86-571-87648507; +86-571-87953149

^bCollege of Chemical and Biological Engineering, Zhejiang University, Hangzhou 310027, China



carbon source for the fabrication of porous carbon matrix. Subsequent to the construction of the $\text{Co}(\text{polypyrrole})_2(\text{NO}_3)_2$ coordination, ORR catalyst (Co-pyrrole/MPC) was prepared by spray-drying the precursor suspension containing glucose, $\text{Co}(\text{polypyrrole})_2(\text{NO}_3)_2$, and nano- CaCO_3 as the template, and calcinating under a high-temperature.^{37–40}

The structure of $\text{Co}(\text{polypyrrole})_2(\text{NO}_3)_2$ precursor was investigated through a series of material characterizations, while the catalytic performance of the product catalyst (Co-pyrrole/MPC) was evaluated by electrochemical analyses in three-electrode configuration and DBFC.

2. Method and procedures

2.1. Catalyst preparation

$\text{Co}(\text{polypyrrole})_2(\text{NO}_3)_2$ precursor was synthesized with a small molar ratio of pyrrole to $\text{Co}(\text{NO}_3)_2$ for utilization of the utmost attachment points in pyrrole. 17.4 g glucose monohydrate and 1.0 mmol of $\text{Co}(\text{NO}_3)_2 \cdot 6\text{H}_2\text{O}$ were dissolved in 50 mL deionized water. The obtained solution was mixed with the emulsion containing 17.4 g nano- CaCO_3 in 20 mL deionized water to form a homogeneous suspension. 2.0 mmol of pyrrole was then added to the suspension dropwise in dark. After stirring for 30 minutes, the suspension was subjected to hydrothermal treatment or spray-drying at 160 °C for preparing catalyst precursor ($\text{Co}(\text{polypyrrole})_2(\text{NO}_3)_2$). The last step was to carbonize the precursor which was performed *via* heating at 900 °C in nitrogen atmosphere for 2 hours. After the template was removed by HCl etching, the porous catalyst (Co-pyrrole/MPC) was then obtained by overnight drying in vacuum at 60 °C. The overall strategy for obtaining the catalyst was showed in Fig. 1.

2.2. Physical characterization

The structure and morphology of the synthesized samples were characterized by X-ray diffraction (XRD) under the use of Rigaku-D/MAX-2550PC diffractometer with Cu- $\text{K}\alpha$ radiation ($\lambda = 1.5406 \text{ \AA}$), scanning electron microscopy (SEM, Zeiss Corp.) operated at 5 kV, and transmission electron microscope (TEM, Hitachi H-9500) operated at 300 kV. The polymerization of Co-coordinated pyrrole was studied by Fourier Transform Infrared Spectroscopy (FTIR) and Co K-edge X-ray absorption near-edge structure



Fig. 2 (a) Glucose dissolved in water, (b) $\text{Co}(\text{NO}_3)_2$ dissolved in water, (c) pyrrole dissolved in water, (d) pyrrole dissolved in glucose solution, (e) pyrrole added to $\text{Co}(\text{NO}_3)_2$ solution, (f) pyrrole added to $\text{Co}(\text{NO}_3)_2$ –glucose solution.

(XANES). The infrared spectra of the synthesized samples in KBr pellets were recorded by Nicolet-IR560 FTIR spectrometer at the spectral resolution of 4 cm^{-1} . XANES measurements were performed on BL15U1 at Shanghai Synchrotron Radiation Facility (SSRF) in China. The XANES data was analysed using a computer program IFEFFIT. Taking tetramethylsilane (TMS) as the internal reference, chemical shifts were displayed in *d* values (ppm). Based on the results of XANES, electron paramagnetic resonance (EPR), and X-ray photoemission spectroscopy (XPS), the effect of catalytic sites on ORR was discussed in details. The N species and their relative contents of the synthesized catalysts were identified by means of PHI-5000C ESCA system (PerkinElmer) with Mg $\text{K}\alpha$ radiation ($h\nu = 1253.6 \text{ eV}$). All XPS spectra referred to the C 1s level of 284.6 eV to correct the peak shift due to the charge accumulation on the sample. XPS Peak 4.1 software was used to fit and deconvolute the raw data.

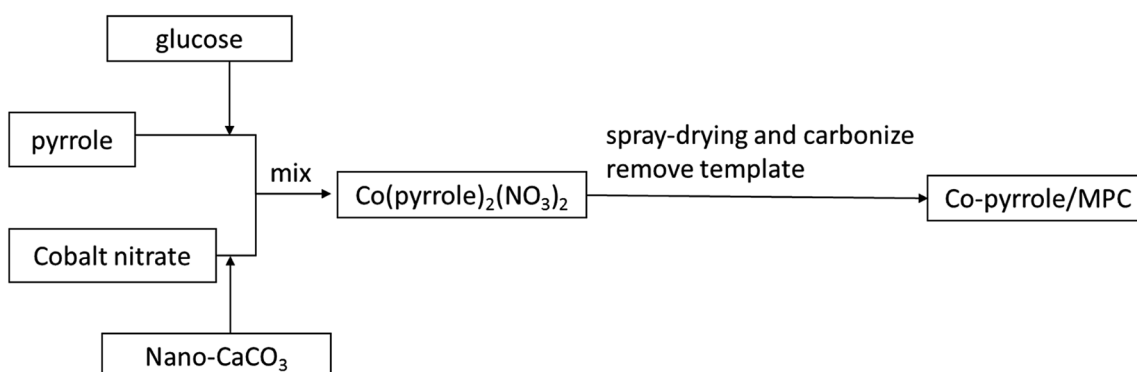


Fig. 1 The scheme of overall strategy for obtaining the catalyst.



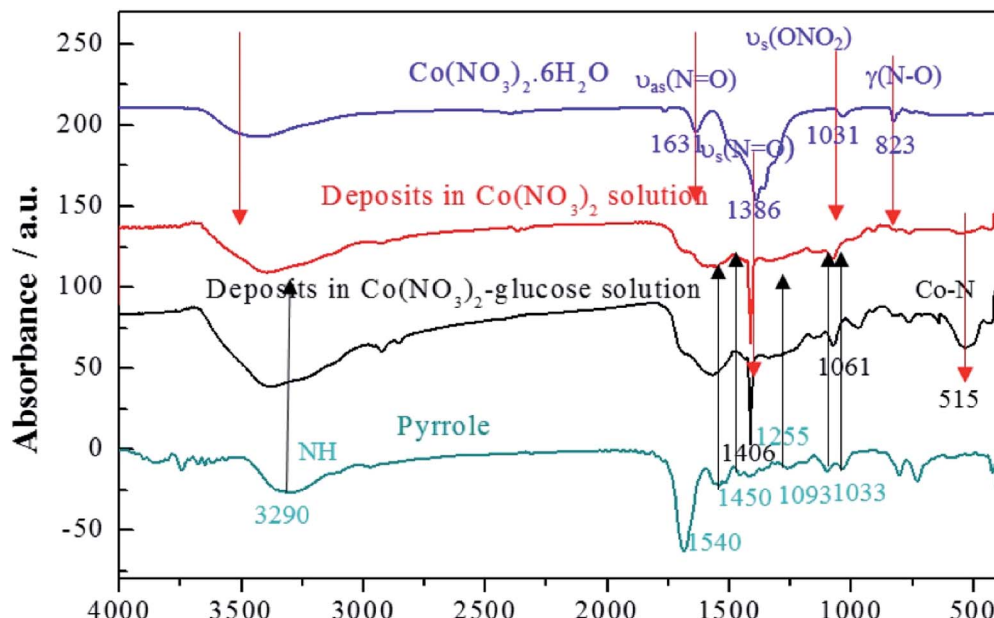


Fig. 3 FTIR spectra of $\text{Co}(\text{NO}_3)_2$, pyrrole, Co-pyrrole and Co-pyrrole-glucose in KBr pellets. The Co-pyrrole and Co-pyrrole-glucose represent the deposits in $\text{Co}(\text{NO}_3)_2$ and $\text{Co}(\text{NO}_3)_2$ -glucose solution, respectively.

2.3. Electrochemical measurements

CHI 1140A electrochemical workstation (CH Instruments) was used to evaluate the electrocatalytic activity of the catalyst in a three-electrode system. The homogenous catalyst ink was formed by mixing 8.0 mg catalyst sample, 0.2 mL Nafion solution (5 wt%) and 3 mL ethanol by ultrasound. The working electrode consisted of 20 μL catalyst ink loaded onto the glassy carbon electrode (3 mm in diameter) and then dried at room temperature. Calomel electrode (SCE) and Pt-wire electrode in saturated KCl solution were used as reference electrode and counter electrode respectively. The cell and reference electrode

were connected with a salt bridge. The cyclic voltammograms (CVs) were recorded in O_2 -saturated solutions at 25 $^\circ\text{C}$ and the scanning rate was 10 mV s^{-1} in alkaline (0.1 M KOH) and acidic (0.5 M H_2SO_4). According to the pH value of the electrolyte, the potentials were converted to v values vs. reversible hydrogen electrode (RHE).

$$E(\text{V vs. RHE}) = E(\text{V vs. SCE}) + 0.241 + 0.0591 \times \text{pH, at } 25^\circ\text{C} \quad (1)$$

Linear sweep voltammetry (LSV) analysis was performed by rotating disk electrode (RDE) (RDE-2, BASi Inc.). According to the geometric area of the disk electrode, the electron transfer number of ORR (n) is estimated. The approximate K-L equation is as follows:

$$j^{-1} = j_k^{-1} + \{0.62nFA_eC_0D_0^{2/3}\nu^{-1/6}\omega^{1/2}\}^{-1} \quad (2)$$

In which j is the disk current, j_k is the kinetic current, F is the Faraday constant, ω is the rotation angular frequency and n is the number of electrons transferred per O_2 molecule *via* ORR. Published data of O_2 saturated concentration (C_0), diffusion coefficients (D_0) of O_2 in 0.1 M KOH and 0.5 M H_2SO_4 solution, and kinematic viscosity (ν) of 0.1 M KOH and 0.5 M H_2SO_4 solution were used, $F = 96\ 485 \text{ C L}^{-1}$; $D_0 = 1.96 \times 10^{-5} \text{ cm}^2 \text{ s}^{-1}$; $C_0 = 1.15 \times 10^{-3} \text{ mol L}^{-1}$; $\nu = 0.008977 \text{ cm}^2 \text{ s}^{-1}$ (0.1 M KOH), $\nu = 0.01 \text{ cm}^2 \text{ s}^{-1}$ (0.5 M H_2SO_4).^{22,24} RDE CVs were also tested at 25 $^\circ\text{C}$ and a scan rate of 10 mV s^{-1} . The working electrode of RDE was loaded with 5 μL catalyst ink onto the polished glassy carbon electrode and then dried at room temperature.

The performance of the synthesized catalyst was verified in the alkaline fuel cell compared with that of the commercial Pt/XC-72 catalysts (28.6 wt% Pt/C). A test cell with an active area of 6 cm^2

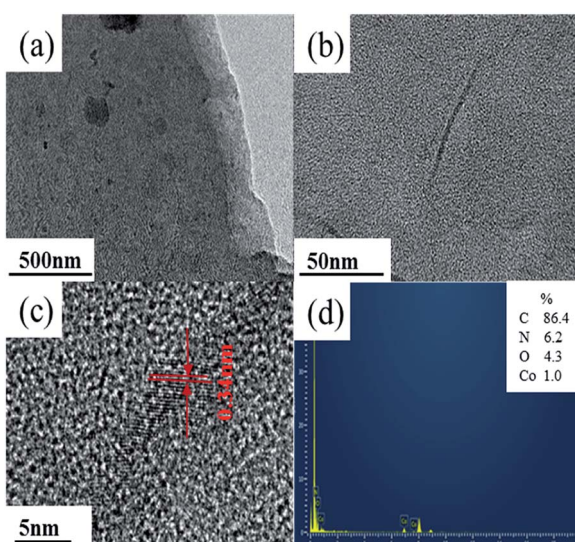


Fig. 4 (a–c) TEM images, (d) EDS spectrum of $\text{Co}(\text{polypyrrole})_2(\text{NO}_3)_2$.

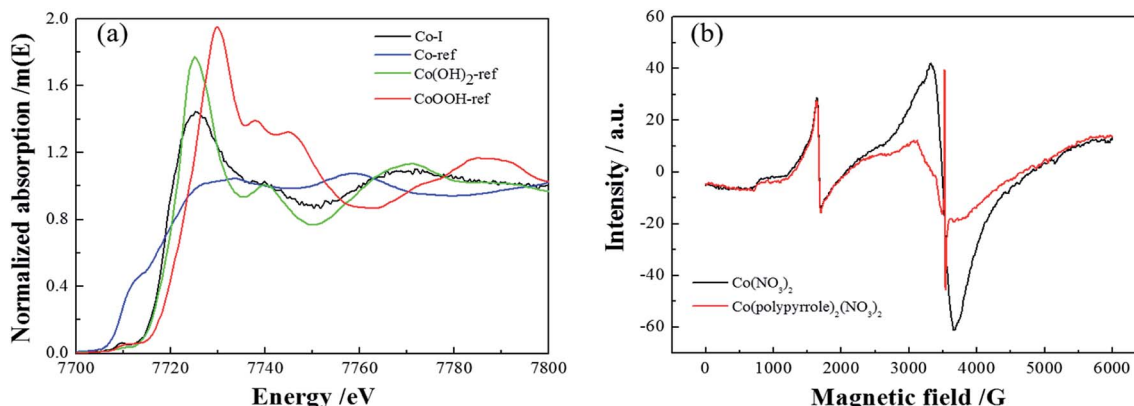


Fig. 5 (a) XANES spectra of $\text{Co}(\text{polypyrrole})_2(\text{NO}_3)_2$ and three reference samples, (b) EPR spectra of $\text{Co}(\text{NO}_3)_2$ and $\text{Co}(\text{polypyrrole})_2(\text{NO}_3)_2$.

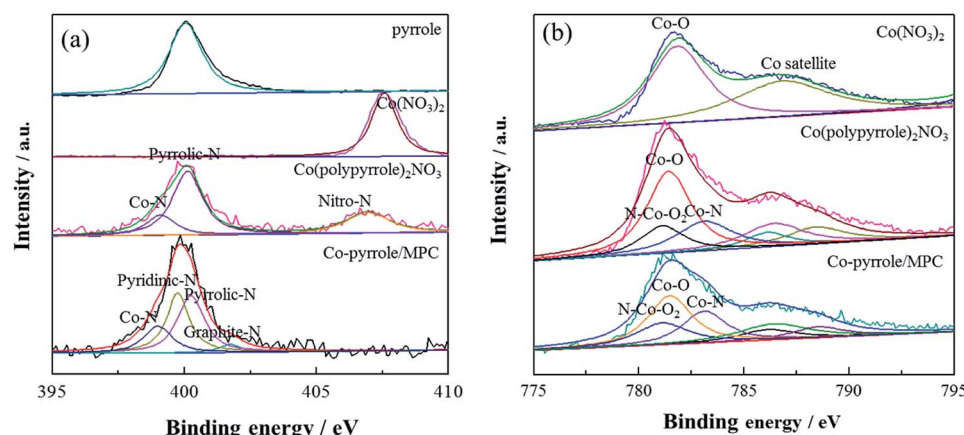


Fig. 6 (a) N 1s and (b) Co 2p XPS spectra of pyrrole, $\text{Co}(\text{NO}_3)_2$, $\text{Co}(\text{polypyrrole})_2(\text{NO}_3)_2$ precursor and Co-pyrrole/MPC catalyst.

was assembled in a direct borohydride fuel cell (DBFC) to evaluate the performance of the synthesized catalyst. The cathode and anode catalyst inks were prepared by mixing the catalyst powder, Nafion solution (5 wt%), deionized water, and ethanol with a mass ratio of 1 : 7 : 3 : 3. The cathode was made from 3.0 mg cm^{-2} synthesized catalyst which was coated onto a piece of hydrophobic carbon cloth and then heated at 130 °C for 2 hours, while the anodes were made from 3.0 mg cm^{-2} commercial Pt/XC-72 catalyst (28.6 wt% Pt) coated onto a piece of Ni foam. Nafion 112 membrane was used as the electrolyte after sequentially boiling in 3 wt% H_2O_2 solution, deionized water for 30 minutes. The alkaline borohydride solution (5 wt% NaBH_4 in 10 wt% NaOH) was used as the fuel to run the cell. The performance of the cell was measured

at 25 °C with a fuel flow rate of 15 mL min^{-1} and a dry O_2 flow rate of 150 mL min^{-1} . The cell performance evaluation system and cell configuration were described in a previous publication.³³

3. Results and discussion

3.1. Characterizations of $\text{Co}(\text{polypyrrole})_2(\text{NO}_3)_2$ precursor

As shown in Fig. 2, it can be observed that glucose and $\text{Co}(\text{NO}_3)_2$ could thoroughly dissolve in water. However, when pyrrole was added into the $\text{Co}(\text{NO}_3)_2$ solution, only few deposits appeared ascribing to the poor solubility of pyrrole. Interestingly, pyrrole could be more easily dissolved in glucose solution, which significantly contributed to the more deposits when pyrrole was

Table 1 Chemical state and percentage content of atomic nitrogen on the surface of $\text{Co}(\text{polypyrrole})_2(\text{NO}_3)_2$ precursor, Co-pyrrole/MPC catalyst

Samples	Co-N 398.9 eV	Pyridinic-N 399.8 eV	Pyrrolic-N 400.3 eV	Graphite-N 401.6 eV	Nitro-N 406.8 eV	Total nitrogen content
$\text{Co}(\text{polypyrrole})_2(\text{NO}_3)_2$	16.6	0	56.6	0	26.8	16.6
Co-pyrrole/MPC	19.9	37.2	39.8	3.1	0	1.75



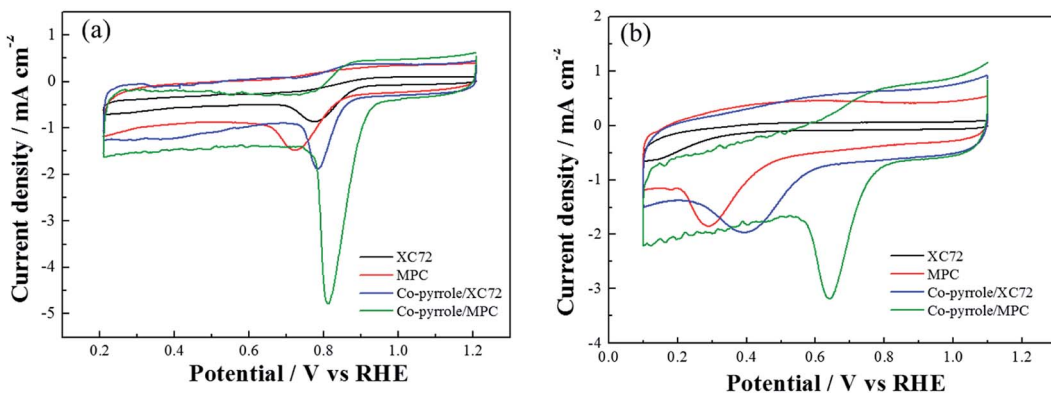


Fig. 7 CVs of MPC, Co-pyrrole/XC72 and Co-pyrrole/MPC in the (a) alkaline (0.1 M KOH), (b) acidic (0.5 M H_2SO_4) O_2 -saturated solutions at 25 °C. Scan rate: 10 mV s^{-1} .

added to the $\text{Co}(\text{NO}_3)_2$ -glucose solution, confirming the hydrotropic effect that intensified the Co-pyrrole coordination. It revealed that glucose can act as a hydrotropic agent to improve the solubility of pyrrole in aqueous media, so as to enhance the Co coordination with pyrrole.

In addition, the FTIR spectra were carried out to indicate the structure of the deposits as shown in Fig. 3. It depicted that cobalt nitrate hexahydrate presented the antisymmetric and symmetric stretching vibrations ($\nu_{\text{as}}(\text{N}=\text{O})$ and $\nu_{\text{s}}(\text{N}=\text{O})$) at 1631 and 1386 cm^{-1} , totally symmetric stretching vibration ($\nu_{\text{s}}(\text{ONO}_2)$) at 1031 cm^{-1} , and bending vibration out of plane ($\gamma(\text{N}-\text{O})$) at 823 cm^{-1} , respectively.^{41,42} Polypyrrole presented the pyrrole ring fundamental vibration ($\nu_{\text{s}}(\text{C}-\text{C})$ and $\nu_{\text{s}}(\text{C}-\text{N})$) at 1540 and 1450 cm^{-1} ,⁴³ the $=\text{C}-\text{H}$ in-plane vibration at 1255, 1093, and 1033 cm^{-1} , and the N-H stretching vibration at 3290 cm^{-1} .⁴² The FTIR results confirmed that the deposits produced in $\text{Co}(\text{NO}_3)_2$ and $\text{Co}(\text{NO}_3)_2$ -glucose solution presented very similar IR absorption with well-maintained nitrate ligand peak. Moreover a strong absorption peak appeared at 515 cm^{-1} , which could be assigned to the Co-N bonding, suggesting the formation of $\text{Co}(\text{polypyrrole})_2(\text{NO}_3)_2$ in both solutions.⁴³ Furthermore, the TEM images (Fig. 4a) showed that $\text{Co}(\text{polypyrrole})_2(\text{NO}_3)_2$ had a microcrystalline structure with obvious lattice fringes under high-resolution TEM

observation, which belonged to neither polypyrrole nor cobalt nitrate. Furthermore, the EDS measurement demonstrated the $\text{Co}(\text{polypyrrole})_2(\text{NO}_3)_2$ with a Co : N : O atom ratio of 1 : 4 : 6, which differed from that of $\text{Co}(\text{NO}_3)_2$ (1 : 2 : 6) but well matched ratio in form of $\text{Co}(\text{polypyrrole})_2(\text{NO}_3)_2$ with a very different morphology from the polypyrrole. So all these results confirmed that the reaction of polypyrrole with cobalt nitrate produced new substance which was supposed to be $\text{Co}(\text{polypyrrole})_2(\text{NO}_3)_2$.

Next, more characterizations were applied to verify the compound. Firstly, Fig. 5a compared the XANES spectra of $\text{Co}(\text{polypyrrole})_2(\text{NO}_3)_2$ precursor and three reference samples, Co, $\text{Co}(\text{OH})_2$ and CoOOH . The coordination environment of Co in the precursor could be determined by comparing the spectrum of the tested sample with those of the references. It could be perceived that the spectrum of $\text{Co}(\text{polypyrrole})_2(\text{NO}_3)_2$ was similar to that of standard sample $\text{Co}(\text{OH})_2$, indicating that most of Co in the precursor existed in the form of cobalt divalent. Fig. 5b presented the EPR spectra of cobalt nitrate and the $\text{Co}(\text{polypyrrole})_2(\text{NO}_3)_2$ precursor. Strong resonance peaks could be clearly observed for both $\text{Co}(\text{NO}_3)_2$ and $\text{Co}(\text{polypyrrole})_2(\text{NO}_3)_2$ with a *g* value of 2.0108 and 2.0007, respectively, indicating the existence of unpaired electrons and the similar valence state of Co in these compounds.

Then, XPS experiment was carried out to further identify the composition of the compound. The N 1s spectrum of $\text{Co}(\text{polypyrrole})_2(\text{NO}_3)_2$ confirmed the existence of Co-N (at 398.9 eV) and pyrrolic N (at 400.3 eV) existence⁴⁴ in addition to $-\text{NO}_2$, as shown in Fig. 5a. The pyridinic nitrogen and Co-N_x structure had been extensively considered as catalytic centers, which was expected to boost the according ORR performance. XPS results showed that graphite-N had the weakest electron yield (sp^2 hybridization) with a characteristic peak at 401.6 eV. The lone

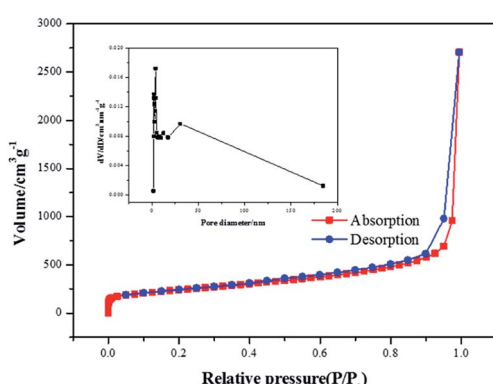


Fig. 8 N_2 adsorption-desorption isotherm and pore size distribution curve of Co-pyrrole/MPC.

Table 2 The BET data of Co-pyrrole/MPC

Sample	Surface area ($\text{m}^2 \text{g}^{-1}$)	Pore volume ($\text{cm}^3 \text{g}^{-1}$)	Pore diameter (nm)
Co-pyrrole/MPC	833.892	6.335	30.178



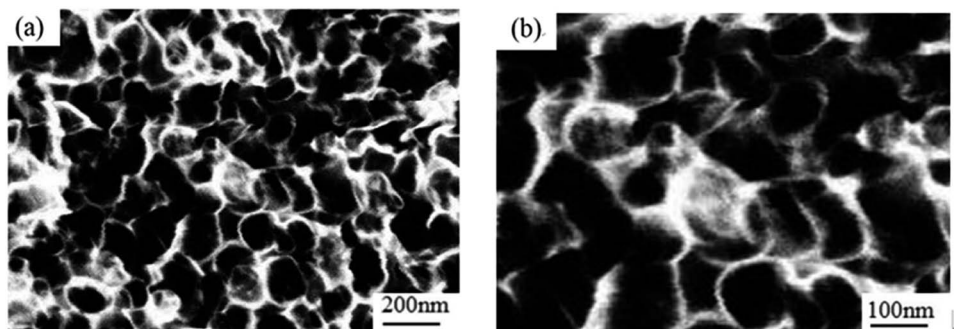


Fig. 9 The SEM images of Co-pyrrole/MPC.

electrons of pyrrolic-N participated in the conjugation on the ring, the hydrogen bond increased the electron concentration on the nitrogen, pyrrolic-N had a peak of 400.3 eV. However, the lone pair of pyridinic-N did not participate in the conjugation on the ring, so it had a higher electron concentration than pyrrolic-N, its peak position was lower than pyrrolic-N. The peak position of Co-N was 398.9 eV, which had higher electron concentration than pyridinic-N. As was shown in Fig. 6a that the coordination compound $(Co(pyrrole)_2(NO_3)_2$) contained two chemical states of nitrogen, *i.e.*, $-NO_2$ with high N 1s binding energy and Co-N with low binding energy. After heat treatment, Co-pyrrole/MPC catalyst was obtained. According to the spectra of Co-pyrrole/MPC, the peak of $-NO_2$ disappeared, and most of the Co-N bonds and residual pyrrolic-N were retained. Quantitative analysis showed that compared with $(Co(pyrrole)_2(NO_3)_2$), the obtained catalyst from heat treatment had more Co-N and pyridinic-N active sites (Table 1), so the Co-pyrrole/MPC catalyst gave great potential to show better catalytic performance for oxygen reduction. In addition, the Co 2p spectrum showed that Co in $(Co(pyrrole)_2(NO_3)_2$ also displayed obvious satellite peaks of cobalt bivalent, indicating that the valence state of cobalt was not changed by coordination and the peaks at 781.3 eV and 783.3 eV corresponding to Co-O bond and Co-N bond respectively. The electron concentration of Co(II) in N-Co-O₂ increased due to the coordination of lone pairs of electrons on pyrrolic-N with -Co-O₂, so Co 2p formed the overlapping peaks of N-Co-O₂, Co-O and Co-N. The peak area of Co-O was twice as that of Co-N or N-Co-O₂, as is shown in Fig. 6b. After heat treatment, the spectra of Co-pyrrole/MPC catalyst showed that the area of Co-O and N-Co-O₂ decreased relatively, but the area of Co-N peak increased, which indicated that more Co-N bonds were formed after heat treatment. Therefore, a new compound was produced based on the above results. And according to the XPS, XANES and EPR tests of the precursor, the valence state of cobalt in

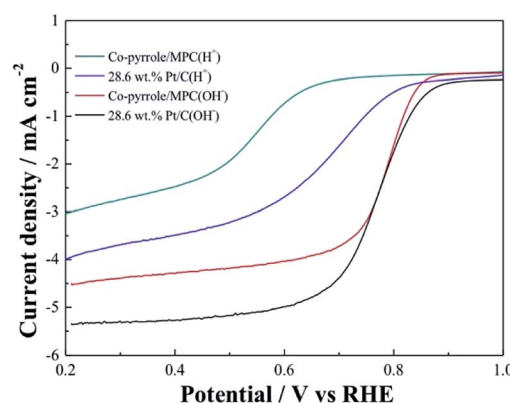
the precursor was still bivalent. Therefore, we suspected that the structure of the $Co(polyppyrrole)_2(NO_3)_2$ precursor was that cobalt nitrate was connected with nitrogen on two pyrrole rings to form a Co-N₂ structure. In an ideal state, pyrrole polymerized while coordinated with cobalt, and finally formed a precursor with double-chain structure.

3.2. Electrochemical properties of Co-pyrrole/MPC catalyst

In order to prove the excellent catalytic performance of catalysts for ORR, different electrochemical properties were tested. Fig. 7 showed the CVs of XC72, MPC, Co-pyrrole/XC72 and the synthesized Co-pyrrole/MPC catalyst in both alkaline and acidic O₂-saturated solutions. It can be seen from the CV curves that both the initial reduction potential and peak current density of Co-pyrrole/MPC were the highest among the four catalysts. As carbon support, XC72 and MPC both showed low catalytic activity, however, the surface area of MPC could reach to nearly 1000 m² g⁻¹, meanwhile, that of XC72 was only around 200 m² g⁻¹,⁴⁵ so that the MPC catalyst can carry more catalytic sites than XC72, which makes MPC catalysts show higher catalytic activity. The N₂ adsorption-desorption isotherm and pore size distribution curve of Co-pyrrole/MPC was showed in Fig. 8, the specific data was listed in Table 2. As the SEM images showed in Fig. 9, Co-pyrrole/MPC contained a large number of pores,

Table 3 The catalytical activity of other catalysts in CV tests⁴⁶

Catalysts	Initial reduction potential (V)	Peak current density (mA cm ⁻²)
Co/P25/NC	0.79	4.31
1 wt% Pt/C	0.75	2.71
20 wt% Pt/C	0.92	2.94

Fig. 10 RDE LSVs of Co-pyrrole/MPC and 28.6 wt% Pt/C in the alkaline (0.1 M KOH) and acidic (0.5 M H₂SO₄) O₂-saturated solutions at 25 °C at a rotation rate of 1600 rpm. Scan rate: 10 mV s⁻¹.

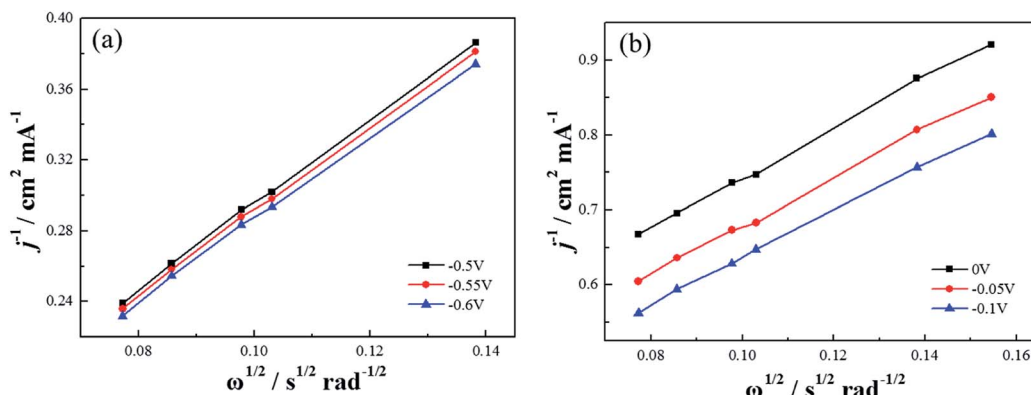


Fig. 11 The K-L plots of Co-pyrrole/MPC in the (a) alkaline (0.1 M KOH), (b) acidic (0.5 M H₂SO₄) O₂-saturated solutions at 25 °C. Scan rate: 10 mV s⁻¹.

which had a larger specific surface area to support more catalytic active centers. In alkaline electrolyte, the initial reduction potential and peak current density of Co-pyrrole/MPC catalyst were 0.9 V and 5 mA cm^{-2} respectively, while in acidic electrolyte, those were 0.8 V and 3.5 mA cm^{-2} . Compared with other articles, the results showed that Co-pyrrole/MPC had relatively high catalytic activity (Table 3).⁴⁶ According to the RDE curves (Fig. 10), the initial reduction potential and peak current density of 28.6 wt% Pt/C were both slightly higher than those of Co-pyrrole/MPC in acidic electrolyte. However, in alkaline electrolyte, 28.6 wt% Pt/C and Co-pyrrole/MPC had similar initial reduction potential.

Based on the K-L equation (eqn (2)) and the RDE LSV results at rotation rates of 500, 900, 1000, 1300, 1600 rpm in alkaline electrolytes and 400, 500, 900, 1000, 1300, 1600 rpm in acidic electrolytes (Fig. 11), the calculated n values for Co-pyrrole/MPC were 3.89 and 2.86 respectively, the result in alkaline electrolyte was close to that for Pt/XC-72 ($n = 4$), revealing that Co-pyrrole/MPC was a high-performance non-Pt catalyst which had a great possibility to replace Pt/C as a cathode catalyst in alkaline electrolyte.

Similar to Pt/C, Co-pyrrole/MPC had higher catalytic activity in alkaline electrolyte than that in acidic electrolyte. The

performance of Co-pyrrole/MPC was further verified in an alkaline fuel cell (e.g. DBFC). The electrochemical performance of the DBFC using Co-pyrrole/MPC as the cathode catalyst was shown in Fig. 12a. A peak power density of 325 mW cm^{-2} was achieved at ambient conditions, which was higher than that with commercial 28.6 wt% Pt/C catalyst (260 mW cm^{-2}). Moreover, Co-pyrrole/MPC demonstrated a good long-term polarization stability in alkaline electrolytes as shown in Fig. 12b.

As is shown in Table 4, compared with similar materials in the previous articles, Co-pyrrole/MPC catalyst had much higher power intensity.⁴⁷⁻⁵⁰



The results showed that the ORR currents and potentials of Co-pyrrole/MPC catalyst in alkaline electrolyte were higher than those in acidic electrolyte. The total reaction formulas of ORR in alkaline and acidic electrolyte are shown in eqn (3) and (4). It was considered that the electrophilic Co(II) could draw nucleophilic dioxygen but repel the electrophilic proton, such as the

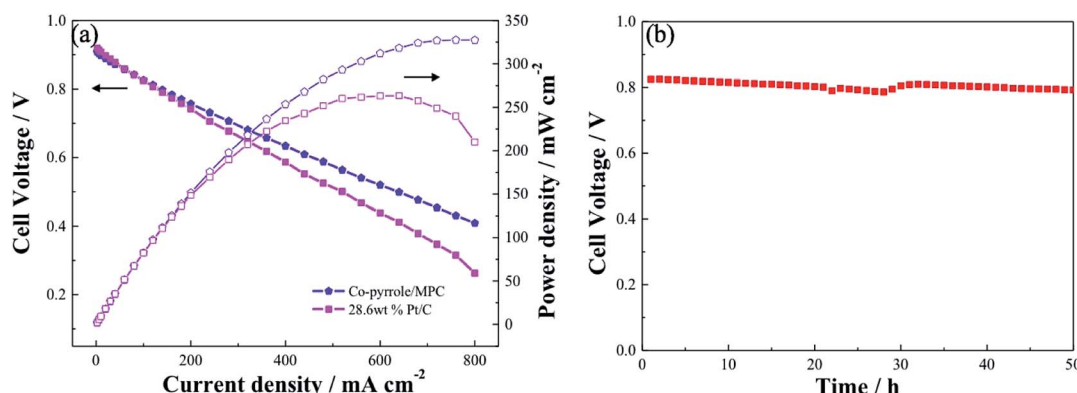


Fig. 12 (a) Performance comparison of DBFCs using Co-pyrrole/MPC and 28.6 wt% Pt/C as the cathode catalyst at ambient conditions, (b) polarization stability of the Co-pyrrole/MPC in the DBFC. Catalyst loading in cathode and anode: 3 mg cm^{-2} , anode catalyst: 28.6 wt% Pt/C, electrolyte: Nafion 112. Fuel: 5 wt% NaBH₄ and 10 wt% NaOH solution at a flow rate of 15 mL min^{-1} . Dry O₂ at 150 mL min^{-1} .



Table 4 The electrochemical performance of similar catalysts in the previous articles^{47–53}

Cathode	Anode	Temperature (°C)	Power intensity (mW cm ⁻²)
FeS-PPy-BP	20 wt% Pt/C	60	140.5
Co-IAA/MPC	20 wt% Pt/C	25	178
Au(Co)/TiO ₂ -NTs	20 wt% Pt/C	25	217
FeIM/ZIF-8	20 wt% Pt/C	80	287
Pt/C	Ni-Pt/C	55	140
CoO nanorods/C	Co(OH) ₂ -PPy/Bp	30	248
CoOOH-PPy/C	Co(OH) ₂ -PPy/Bp	25	101
FeS-PPy/Bp	Pt/C	60	140.5

protons in eqn (4). Most protons were absorbed at nucleophilic centers such as O in Co–O, and the separation and adsorption of dioxygen and protons produced space stereoscopic effect, which hindered the reaction of dioxygen with protons, contributing to the large polarization of ORR in acidic electrolyte, which led to the low electrochemical performance.⁵¹ Co-pyrrole/MPC showed high catalytic activity in alkaline electrolyte. Pyrolysis can effectively increase the number of Co-N₂ and pyridinic-N which were considered as the catalytic sites, as enhanced the ORR activity. Double-chain structure of the catalyst contributed to a better electrochemical stability. According to the results of electrochemical tests, Co-pyrrole/MPC is definitely a promising ORR catalyst to replace Pt.

4. Conclusions

Taking advantages of coordination and polymerization capability of pyrrole, we used pyrrole as the ligand to coordinate Co(II) to prepare Co(pyrrole)₂(NO₃)₂ as catalyst precursor. By utilizing the higher specific surface area of MPC, the catalyst with MPC could support more active centers.

The MPC-supported N-containing cobalt catalyst (Co-pyrrole/MPC) which was synthesized *via* pyrolysis of precursor containing glucose, pyrrole and cobalt nitrate had high catalytic performance. During the preparation process, in addition to the carbon sources, glucose could also provide increased solubility of pyrrole in water, which enabled a high-efficiency coordination between pyrrole and Co(II) upon the polymerization. Co-pyrrole/MPC catalyst exhibited high ORR activity in alkaline electrolytes, the initial reduction potential reached 0.9 V and the peak current density reached 5 mA cm⁻² at room temperature. The excellent catalytic performance was further examined in the direct borohydride fuel cell, the peak power density reached 325 mW cm⁻² at room temperature.

Conflicts of interest

There are no conflicts to declare.

Acknowledgements

This work was financially supported by the National Natural Science Foundation of China (Grant No. 21776245).

References

- X. L. Tian, X. Zhao, Y. Q. Su, L. J. Wang, H. M. Wang, D. Dang, B. Chi, H. F. Liu, E. J. M. Hensen, X. W. Lou and B. Y. Xia, *Science*, 2019, **366**, 850–856.
- L. Elbaz and F. H. Garzon, *J. Electroanal. Chem.*, 2013, **700**, 65–69.
- C. Gu and C. Shannon, *J. Mol. Catal. A: Chem.*, 2007, **262**, 185–189.
- Y. Gorlin and T. F. Jaramillo, *J. Mol. Catal. A: Chem.*, 2010, **132**, 13612–13614.
- R. Jasinski, *Nature*, 1964, **201**, 1212–1213.
- V. Goellner, C. Baldizzone, A. Schuppert, M. T. Sougrati, K. Mayrhofer and F. Jaouen, *Phys. Chem. Chem. Phys.*, 2014, **16**, 18454–18462.
- M. Kato, K. Kimijima, M. Shibata, H. Notsu, K. Ogino, K. Inokuma, N. Ohta, H. Uemura, N. Oyaizu, T. Ohba, S. Takakusagi, K. Asakura and I. Yagi, *Phys. Chem. Chem. Phys.*, 2015, **17**, 8638–8641.
- Z. P. Li, Z. X. Liu, K. N. Zhu, Z. Li and B. H. Liu, *J. Power Sources*, 2012, **219**, 163–171.
- Z. X. Liu, B. H. Liu and Z. P. Li, *Int. J. Hydrogen Energy*, 2014, **39**, 5689–5695.
- R. Bashyam and P. Zelenay, *Nature*, 2006, **447**, 63–66.
- V. Nallathambi, J. W. Lee, S. P. Kumaraguru, G. Wu and B. N. Popov, *J. Power Sources*, 2008, **183**, 34–42.
- L. Gang, X. Li, P. Ganesan and B. N. Popov, *Appl. Catal., B*, 2009, **93**, 156–165.
- Y. R. Liu, B. P. Lin, D. Li, X. Q. Zhang, Y. Sun and H. Yang, *J. Porous Mater.*, 2014, **21**, 933–938.
- E. S. Toberer, T. D. Schladt and R. Seshadr, *J. Am. Chem. Soc.*, 2006, **128**, 1462–1463.
- J. Kim, J. Jang, D. Peck, B. Lee, S. Yoon and D. Jung, *J. Electroanal. Chem.*, 2016, **768**, 34–40.
- D. Khalafallah, O. Y. Alothman, H. Fouad and K. A. Khalil, *J. Electroanal. Chem.*, 2018, **809**, 96–104.
- A. Sarapuu, L. Samolberg, K. Kreek, M. Koel, L. Matisen and K. Tammeveski, *J. Electroanal. Chem.*, 2016, **746**, 9–17.
- C. Q. Yang, S. S. Jie, R. L. Zhu, N. D. Zhang, J. Q. Wang and Z. G. Liu, *Chemistryselect*, 2017, **2**, 4255–4260.
- L. Q. Gao, M. L. Xiao, Z. Jin, C. P. Liu, J. B. Zhu, J. J. Ge and W. Xing, *J. Energy Chem.*, 2018, **27**, 1668–1673.
- C. Zhang, J. Liu, Y. Ye, Z. Aalam, R. Brydson and C. Liang, *ACS Appl. Mater. Interfaces*, 2018, **10**, 2423–2429.
- Z. Chen, D. C. Higgins, H. S. Tao, R. S. Hsu and Z. W. Chen, *J. Phys. Chem. C*, 2009, **113**, 21008–21013.
- M. H. Robson, A. Serov, K. Artyushkova and P. Atanassov, *Electrochim. Acta*, 2012, **90**, 656–665.
- C. W. B. Bezerra, Z. Lei, K. C. Lee, H. S. Liu, A. L. B. Marques, E. P. Marques, H. J. Wang and J. J. Zhang, *Electrochim. Acta*, 2008, **53**, 4937–4951.
- D. Zhang, D. Chi, T. Okajima and T. Ohsaka, *Electrochim. Acta*, 2007, **52**, 5400–5406.
- S. Yamazaki, *Coord. Chem. Rev.*, 2018, **373**, 148–166.
- G. L. Mcpherson and P. J. J. Losavio, *Inorg. Chem.*, 1975, **14**, 2116–2120.



27 D. W. James and W. H. Leong, *Chem. Commun.*, 1968, 1415–1417.

28 E. J. Corey and J. A. Katzenellenbogen, *J. Am. Chem. Soc.*, 1969, **91**, 1851–1852.

29 H. Q. Wang, L. L. Wei, J. T. Liu and J. Q. Shen, *Int. J. Hydrogen Energy*, 2020, **45**, 4481–4489.

30 X. H. Lv, Z. X. Xiao, H. Y. Wang, X. L. Wang, L. L. Shan, F. L. Wang, C. Y. Wei, X. J. Tang and Y. L. Chen, *J. Energy Chem.*, 2020, **20**, 30453–30458.

31 H. W. Zhao, T. Y. Xing, L. X. Li, X. Geng, K. Guo, C. G. Sun, W. M. Zhou, H. M. Yang, R. F. Song and B. G. An, *Int. J. Hydrogen Energy*, 2019, **44**, 25180–25187.

32 H. Y. Qin, Z. X. Liu, S. J. Lao, J. K. Zhu and Z. P. Li, *J. Power Sources*, 2010, **195**, 3124–3129.

33 H. Y. Qin, Z. X. Liu, L. Q. Ye, J. K. Zhu and Z. P. Li, *J. Power Sources*, 2009, **192**, 385–390.

34 Y. Makoto, Y. Aritomo, I. Hisayuki, T. Ken, Y. Masakuni and O. Kenichi, *Chem. Mater.*, 2005, **17**, 4278–4281.

35 K. Lee, Z. Lei, H. Lui, R. Hui, Z. Shi and J. Zhang, *Electrochim. Acta*, 2009, **54**, 4704–4711.

36 T. Viswanathan and T. Richardson, *Ind. Eng. Chem. Res.*, 1989, **23**, 644–647.

37 A. Vinu, Z. Kazi, P. Srinivasu, M. Miyahara, S. Anandan, N. Gokulakrishnan, T. Mori, K. Ariga and V. V. Balasubramanian, *J. Mater. Chem.*, 2007, **17**, 1819–1825.

38 K. P. Gierszal, M. Jaroniec, C. D. Liang and S. Dai, *Carbon*, 2007, **45**, 2171–2177.

39 A. H. Janssen, I. Schmidt, C. J. H. Jacobsen, A. J. Koster and K. P. de Jong, *Microporous Mesoporous Mater.*, 2003, **65**, 59–75.

40 C. R. Zhao, W. K. Wang, Z. H. Yu, H. Zhang, A. B. Wang and Y. S. Yang, *J. Mater. Chem.*, 2010, **20**, 976–980.

41 L. Chierici and G. P. Gardini, *Tetrahedron*, 1966, **22**, 53–56.

42 L. Jing and M. Wan, *J. Mater. Chem.*, 2001, **11**, 404–407.

43 G. P. GlasPELL, P. W. Jagodzinski and A. Manivannan, *J. Phys. Chem. B*, 2004, **108**, 9604–9607.

44 W. Geng, Y. Kumabe, T. Nakajima, H. Takanashi and A. Ohki, *Fuel*, 2009, **88**, 644–649.

45 G. R. Li, Z. P. Li and Z. Lin, *Energy Storage Sci. Technol.*, 2016, **5**, 135–148.

46 K. J. Miyake, T. Takemura, A. Gabe, Y. X. Zhu, M. Ota, Y. Shu, Y. Hirota, Y. Uchida, S. Tanka, M. Katayama, Y. Inada and N. Nishiyama, *Electrochim. Acta*, 2019, **296**, 867–873.

47 B. H. Liu, L. T. Dou, F. He, J. Yang and Z. P. Li, *RSC Adv.*, 2016, **6**, 19025–19033.

48 M. Abdolmaleki and M. G. Hosseini, *Fuel Cells*, 2017, **17**, 321–327.

49 A. Balčiūnaitė, L. Tamašauskaitė-Tamašiūnaitė, D. M. F. Santos, A. Zabielaite, A. Jagminienė, I. Stankevičienė and E. Norkus, *Fuel Cells*, 2017, **17**, 690–697.

50 D. Zhao, J. L. Shui, C. Chen, X. Q. Chen, B. M. Reprogile, D. P. Wang and D. J. Liu, *Chem. Sci.*, 2012, **3**, 3200–3205.

51 J. J. Jia, X. X. Li, H. Y. Qin, Y. He, H. L. Ni and H. Z. Chi, *J. Alloys Compd.*, 2019, **820**, 153065–153071.

52 Y. He, C. Zhu, K. J. Chen, J. Wang, H. Y. Qin, J. B. Liu, S. Yan, K. Yang and A. G. Li, *J. Power Sources*, 2017, **339**, 13–19.

53 L. X. Lin, H. Y. Qin, J. K. Jia, Z. G. Ji, H. Z. Chi, H. L. Ni, J. Wang, Y. He and J. B. Liu, *J. Alloys Compd.*, 2018, **769**, 136–140.

